Full length article

Effect of vanadium micro-alloying on the microstructural evolution and creep behavior of Al-Er-Sc-Zr-Si alloys

Dinc Erdeniz [a, *], Wahaz Nasim [b], Jahanzaib Malik [b], Aaron R. Yost [a], Sally Park [a], Anthony De Luca [a], Nhon Q. Vo [c], Ibrahim Karaman [b], Bilal Mansoor [d], David N. Seidman [a, c, e], David C. Dunand [a, c]

[a] Department of Materials Science and Engineering, Northwestern University, 2220 Campus Drive, Evanston, IL 60208, USA
[b] Department of Materials Science and Engineering, Texas A&M University, 575 Ross Street, College Station, TX 77843, USA
[c] NanoAl LLC, 8025 Lamon Avenue, Ste 446, Skokie, IL 60077 USA
[d] Mechanical Engineering Program, Texas A&M University at Qatar, Education City, Doha, Qatar
[e] Northwestern University Center for Atom-Probe Tomography, Northwestern University, 2220 Campus Drive, Evanston, IL 60208, USA

ARTICLE INFO

ABSTRACT

Al-Er-Sc-Zr-Si alloys, strengthened by $L1_2$-ordered, coherent $Al_3(Er,Sc,Zr)$ nanoscale precipitates, can be used for automotive and aerospace applications up to 400 °C. Vanadium, due to its small diffusivity in aluminum and its ability to form $L1_2$-ordered tri-aluminide precipitates, is a possible micro-alloying addition for further improving the service temperature of these alloys. Moreover, vanadium-containing $Al_3(Er,Sc,Zr,V)$ precipitates are anticipated to have a smaller lattice parameter mismatch with the matrix, thereby improving the alloy's coarsening resistance. In this study, the temporal evolution of microstructural and mechanical properties of an Al-0.005Er-0.02Sc-0.07Zr-0.06Si alloy micro-alloyed with V are investigated utilizing isochronal, isothermal and double-aging treatments and compared to the results obtained from an alloy that does not contain V, but otherwise has the same composition. Both isochronal and isothermal aging treatments reveal slower precipitation and coarsening kinetics for the V-containing alloy. A peak microhardness value of ~600 MPa is obtained after a double-aging treatment at 350 °C/16 h, followed by aging at 400 °C for 12 h. Transmission electron microscopy reveals a duplex-size precipitate microstructure, with the smaller precipitates having a mean radius <3 nm. Despite the expectation of a reduced creep resistance due to a lower precipitate/matrix lattice mismatch, both alloys have similar creep behavior at 400 °C, characterized by a threshold stress of 7.5 and 8 MPa under peak-aged and over-aged conditions, respectively. Thus, micro-additions of V to an Al-Er-Sc-Zr-Si alloy lead to enrichment of V in the $Al_3(Er,Sc,Zr,V)$ nano-precipitates, improving their coarsening resistance without deteriorating their ability to block dislocations under creep at 400 °C.

© 2016 Acta Materialia Inc. Published by Elsevier Ltd. All rights reserved.

1. Introduction

Castable, heat-treatable aluminum alloys are utilized widely in a number of applications; including automotive, aerospace, and power transmission, due to a combination of desired properties, such as low density, high specific strength, good oxidation resistance, high electrical conductivity, and relatively low cost. Their strength and creep resistance is, however, low at temperatures above ~250 °C, due to precipitate dissolution and/or coarsening, which limits the utilization of these alloys, in as-cast or wrought conditions, for high-temperature applications.

Al-Sc alloys, strengthened with $L1_2$-ordered Al_3Sc precipitates, provide a promising alternative to overcome this problem [1–11]. These alloys can be utilized at service temperatures up to 300 °C; however, due to the limited availability of Sc they are rather expensive. There has been extensive research focused on identifying other alloying elements that can further increase the service temperature and replace some of the Sc content, thereby rendering the alloys less expensive. The main requirement for any of these potential substitute alloying elements is that they form $L1_2$-ordered tri-aluminide precipitates. Rare earth (RE) elements, such as Er, Tm, Lu and Yb, are known to replace some of the Sc in the $Al_3(Sc,RE)$

phase [11–14] and research has demonstrated that Er is the most effective and the least expensive RE [11,12]. However, due to the higher diffusivity of Er in Al compared to Sc, it commences to precipitate at lower temperatures (ca. 250–275 °C), which does not improve the service temperature. Also due to the difference in the diffusivities of Er and Sc they form a core/shell precipitate structure, where Al_3Er forms a core and $Al_3(Sc,Er)$ forms a shell [11]. As a result, the high temperature creep resistance of Al-Er-Sc alloys improves significantly compared to binary Al-Sc alloys, due to a larger lattice parameter mismatch between the precipitate shell and the Al matrix [9,15].

On the other hand, some of the transition metal elements, Zr, Ti, or Hf, substitute for Sc in $L1_2$-ordered-precipitates [16]. Specifically, Zr is known to significantly improve the coarsening resistance, which is attributed to its low diffusivity. In Al-Er-Sc-Zr alloys, Zr promotes the formation of the final shell of core/shell/shell precipitates, which serves as an effective diffusion barrier for coarsening at elevated temperatures [4,7]. These alloys can be used at service temperatures as high as 400 °C [7].

Furthermore, Si is one of the main impurities in Al and micro-alloying with it in these alloys offer several benefits and can enable the use of less expensive commercial-purity aluminum (99.9%). It can increase the precipitate number density by promoting heterogeneous nucleation [8]. Additionally, Si increases the precipitation kinetics, thereby; reducing the aging time required to achieve peak microhardness [8].

The objective of this research is to investigate the effects of V addition on the coarsening- and creep-resistant properties of Al-Er-Sc-Zr-V-Si alloys. Vanadium forms metastable, $L1_2$-ordered Al_3V precipitates and has a diffusivity in Al that is even lower than that of Zr [17]. Therefore, in this context, V has the potential to either create another precipitate shell or modify the Zr-rich shell by forming $Al_3(Zr,V)$. Vanadium is expected to decrease lattice parameter misfit between the precipitates and the Al matrix; hence, its effect on creep resistance must be carefully studied [18]. On the other hand, V is expected to reduce the solubility of Zr in Al, and this may cause the formation of primary precipitates during solidification, which may result in a small grain size, creating an undesirable microstructure for high-temperature creep resistance. We performed isochronal, isothermal, and double aging studies to understand the microstructural evolution and mechanical properties of an Al-Er-Sc-Zr-V-Si alloy, while using an Al-Er-Sc-Zr-Si control alloy to focus on the effects of V additions. Microstructural evolution was studied at four different length scales, utilizing optical microscopy (OM), scanning electron microscopy (SEM), transmission electron microscopy (TEM), and atom-probe tomography (APT). Mechanical properties were studied utilizing Vickers microhardness measurements at room temperature and compression creep experiments at 400 °C. Electrical properties, in particular the electrical conductivity, were also measured at room temperature to evaluate the microstructural evolution as a function of aging time and temperature.

2. Experimental procedures

2.1. Casting and aging treatments

Two alloys with nominal compositions of Al−0.005Er−0.02Sc−0.07Zr−xV−0.06Si at.% (Al−0.031Er−0.033Sc−0.236Zr−xV−0.062Si wt%) were fabricated: a control alloy, Q1, was V-free (x = 0) and an experimental alloy, Q2, was V-bearing (x = 0.08 at.% or 0.15 wt%). Both alloys were prepared from 99.99 at.% pure Al, and master alloys consisting of Al−5.9 wt% Er, Al−2 wt% Sc, Al−8 wt% Zr, Al−5 wt% V, and Al−12.6 wt% Si. Pieces from the above metals and alloys were melted in alumina crucibles at 800 °C in a

resistively heated muffle furnace and stirred five times using alumina rods with a 15 min hold time between each stir. Subsequently, alloys were cast in graphite molds that were preheated to 200 °C and then placed on an ice-cooled copper platen to promote directional solidification. Upon full solidification, which approximately takes 20–30 s, the alloy ingots were quenched into an iced water bath.

Then a homogenization treatment was performed at 640 °C for 4 h, followed by one of the following three aging treatments: (i) isochronal aging treatments over the temperature range of 200–575 °C with 25 °C increments and a 3 h holding time at each temperature; (ii) isothermal aging treatments at 400 and 425 °C for times up to 264 h; and (iii) double-aging treatments, designed to find the peak microhardness conditions, at a primary aging temperature of 300 or 350 °C for 16 h and a secondary aging temperature of 400, 425, or 450 °C for times up to 200 h. All heat treatments were conducted in air and terminated by water quenching.

2.2. Microstructural characterization

The chemical compositions of the as cast ingots were measured by direct-current plasma atomic-emission spectroscopy (DCP-AES) at ATI Wah Chang (Albany, OR) using two samples taken from the top and the bottom of the ingots and also studied by APT [19,20]. All specimens for OM and SEM investigations were prepared using standard metallographic techniques. To reveal the grain structure, select specimens were dip-etched with Poulton's reagent (60 vol% hydrochloric acid + 30 vol% nitric acid + 5 vol% hydrofluoric acid + 5 vol% water) for 30 s. Electrical conductivity (EC) measurements were performed at 120, 240, 480, and 960 kHz (five measurements per frequency) using a Sigmatest 2.069 eddy current instrument (Foerster Instruments, Pittsburgh, PA).

TEM specimens were prepared by cutting ~1.5 mm thick samples with a diamond saw, which were then mechanically ground with SiC papers to a thickness of ~70 μm. Standard 3 mm TEM discs were mechanically punched from the thin foils and twin jet electropolished using a 30 vol% nitric acid and 70 vol% methanol electrolyte solution at −10 °C. A 10 Vdc potential was utilized, which resulted in a current of 70–90 mA. After electropolishing, the specimens were cleaned with methanol. A JEOL JEM-2010 high resolution TEM and a FEI Tecnai G2-F20 ST scanning transmission electron microscope (STEM) were used for sample analysis. Diffraction spots were confirmed with CaRIne Crystallography (CaRIne Crystallography, Senlis, France) and JEMS simulation software (Interdisciplinary Center for Electron Microscopy, Swiss Federal Institute of Technology Lausanne).

APT specimens were prepared by cutting blanks with a diamond saw to ~0.5 × 0.5 × 10 mm^3 dimensions and subsequently electropolished in two stages: (i) coarse electropolishing at 20–25 Vdc using a solution of 10 vol% perchloric acid in acetic acid to form a neck; and (ii) fine polishing at 15–18 Vdc using a solution of 2 vol% perchloric acid in butoxyethanol to dissolve the neck and obtain a tip. Picosecond pulsed ultraviolet (wavelength = 355 nm) laser assisted APT was performed using a LEAP4000X-Si tomograph (Cameca, Madison, WI) at a pulse repetition rate of 500 kHz, a pulse energy of 50 pJ, and a sample temperature of −243 °C. The three-dimensional tomographic data was subsequently analyzed utilizing Cameca's integrated visualization and analysis software (IVAS), version 3.6.8.

2.3. Mechanical testing

Vickers microhardness tests were performed utilizing a Duramin 5 microhardness tester (Struers), employing a 200 g load and a

5 s indentation time. At least 10 indentations were performed on specimens, which were polished to a 1-μm surface finish.

Compressive creep experiments were performed at 400 ± 2 °C on cylindrical samples with a diameter of 9 mm and a height of 18 mm. The samples were heated in a three-zone furnace and the temperature was measured using a K-type thermocouple placed within 1 cm of the specimen. The samples were placed between tungsten carbide platens lubricated with boron nitride. They were subjected to uniaxial compression by Ni-based superalloy rams in a compression cage using dead loads. Sample displacement was monitored with a linear variable displacement transducer with infinite resolution and maximum non-linearity of ±0.25%. A strain rate was obtained by measuring the slope of the strain vs. time plot in the steady-state (secondary) creep regime. When a measurable steady-state strain rate was achieved after a certain duration, the applied load was increased to obtain another steady-state strain rate. Thus, a single specimen provided minimum creep rates for a series of increasing stress levels, at the end of which the total strain did not exceed 10%.

3. Results and discussion

3.1. As-cast and homogenized microstructures

Fig. 1(a) displays the grain structure of the as-cast alloy Q2 with a composition of Al−0.007Er−0.013Sc−0.071Zr−0.074V−0.054Si at.%, close to the nominal composition except for a leaner Sc content, which was verified employing DCP-AES and APT (Tables 1 and 2 for peak- and over-aged conditions). Grains are elongated in shape due to directional solidification. The grain size is relatively coarse (typically ~1−2 mm in width and ~4−8 mm in length), indicating limited formation of primary precipitates during solidification, which are known to nucleate grains. This coarse grain structure is preferred for optimum creep resistance. The SEM image displayed in Fig. 1(b) exhibits ~1 μm size precipitates decorating the grain boundaries in the polished cross-section of a Q2 specimen homogenized at 640 °C for 4 h before aging. Although these precipitates are too small to be analyzed accurately employing EDS, the results revealed a higher peak for Zr in the analyzed volume containing a precipitate compared to the matrix, with all other elements close to the matrix values. This indicates that these particles very likely are Al_3Zr primary precipitates that form during solidification, as also observed in other studies; however, precipitation during homogenization cannot be excluded. A high volume fraction of primary precipitates can have detrimental effects on the creep response of an alloy due to: (i) Zener pinning the grain boundaries, which may result in a fine grain structure - deleterious to creep resistance; and (ii) scavenging Zr and thereby reducing its amount available in the solid solution to form $L1_2$ nano-precipitates - necessary for high temperature creep resistance. The coarse grain structure seen in Fig. 1(a) and microhardness results presented in the following sections suggest that the primary precipitates have a low volume fraction and they do not have a significant effect on the alloy properties.

The verified composition of the control alloy Q1 is Al−0.005Er−0.019Sc−0.068Zr−0.066Si at.%. It possesses a similar grain structure with the presence of Zr-rich primary precipitates visible at the grain boundaries [21].

3.2. Isochronal aging

The evolution of electrical conductivity and microhardness for the isochronal aging treatments for alloys Q1 and Q2 are displayed in Fig. 2(a) and (b), respectively. Fig. 2(a) displays the evolution of electrical conductivity for both alloys, which provides an indirect

evaluation of microstructural changes. In the homogenized state, where the alloying elements are in solid solution, the conductivity is anticipated to have the smallest value. As precipitates nucleate and grow, solute atoms precipitate from the matrix, causing an increase in the conductivity.

Fig. 2(a) shows that the conductivity for the homogenized alloy Q1 is 4−5 MS m^{-1} higher than those for the alloy Q2. Since the only difference between these two alloys is their V concentrations (0 at.% for Q1 and 0.08 at.% for Q2), it is apparent that the V in solid solution significantly reduces the electrical conductivity of aluminum. As the aging treatment temperatures increase, particularly above 500 °C, the precipitates dissolve, therefore reducing the conductivity to nearly its values observed for the homogenized alloy. Another difference between the two alloys is the temperatures where the conductivity value starts to increase. For Q1, first a very small peak is observed at 225 °C, where Er is anticipated to precipitate from the solid solution to form Er-rich $Al_3(Er,X)$ precipitates, with X = Sc associated with small concentrations of Sc co-precipitating [11]. A second small peak is visible at 350 °C, which most likely corresponds to precipitation of Sc-rich $Al_3(Sc,X)$ precipitates and the main peak occurs at 450 °C, where Zr-rich $Al_3(Zr,X)$ precipitates form [4,7,9,10]. There is a plateau between

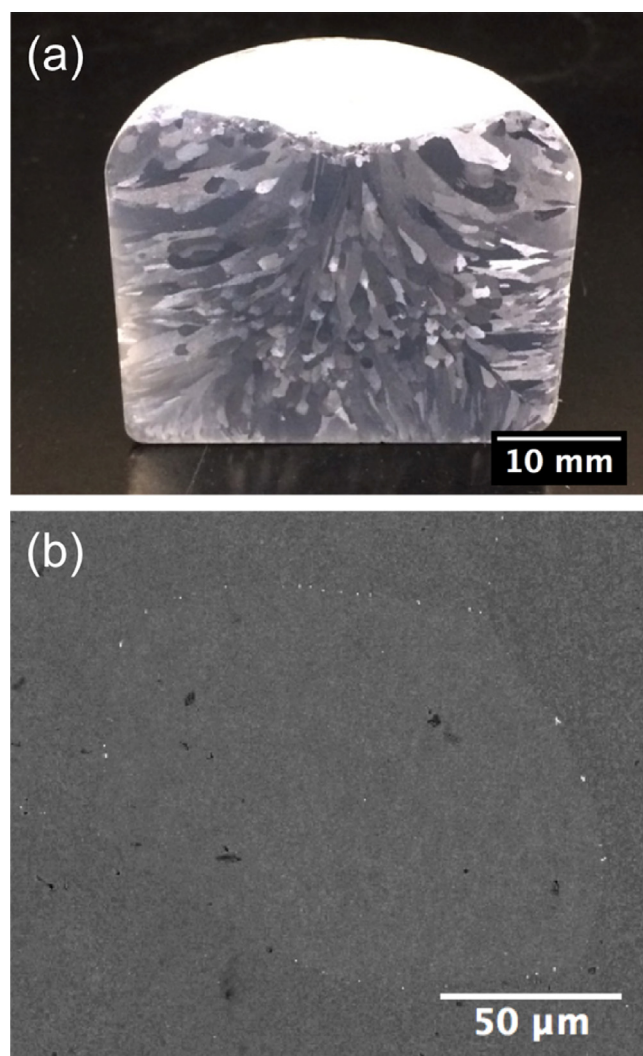**Fig. 1.** (a) An optical micrograph showing the grain structure of as-cast alloy Q2 and (b) SEM image showing primary Al_3Zr precipitates (white particles) decorating grain boundaries in homogenized (640°C/4 h) alloy Q2.

Table 1
Compositions obtained via DCP-AES and APT (tip, matrix, precipitates) for alloy Q2 under peak-aging conditions (350°C/16 h + 400°C/12 h). 62 full and 59 partial precipitates for the peak-aged alloy were analyzed.

Alloy Q2 − Peak aged						
at.%	Al	Er	Sc	Zr	V	Si
Nominal	99.765	0.005	0.02	0.07	0.08	0.06
DCP-AES	99.781	0.007	0.013	0.071	0.074	0.054
APT Tip	99.7588	0.0061	0.0165	0.0578	0.0962	0.0646
APT Matrix	99.8275	0	0.0017	0.013	0.0962	0.0616
APT Precipitates	71.02	2.42	3.13	22.8	0.05	0.58

Table 2
Compositions obtained via DCP-AES and APT (tip, matrix, precipitates) for alloy Q2 under over-aging conditions (350°C/16 h + 450°C/24 h). Three full and 7 partial precipitates for Dataset (DS) #1 and 3 full and 5 partial precipitates for DS #2 were analyzed.

Alloy Q2 − Over aged						
at.%	Al	Er	Sc	Zr	V	Si
Nominal	99.765	0.005	0.02	0.07	0.08	0.06
DCP-AES	99.7721	0.005	0.0174	0.0638	0.0797	0.062
APT Tip DS #1	99.7346	0.0092	0.0425	0.1022	0.0238	0.0877
APT Tip DS #2	99.464	0.0005	0.0492	0.2056	0.1585	0.1221
APT Matrix DS #1	99.8833	0	0.0018	0.0087	0.0238	0.0824
APT Matrix DS #2	99.5542	0.0001	0.0085	0.1579	0.1585	0.1207
APT Precipitates DS #1	77.97	1.25	5.15	14.83	0.03	0.77
APT Precipitates DS #2	75.4	0.15	10.63	13.14	0.14	0.54

425 and 500 °C, very likely due to precipitate coarsening at this temperature range. At higher temperatures, a sharp decrease in electrical conductivity is observed due to precipitate dissolution. For alloy Q2 the conductivity values increase more slowly compared to alloy Q1, which has a single peak between 350 and 425 °C. For Q2 alloy, a similar plateau is observed between 425 and 500 °C, however, the decrease in conductivity at higher temperatures is not as rapid as in Q1. These results indicate slower precipitation kinetics at lower temperatures and enhanced coarsening resistance along with reduced dissolution kinetics at higher temperatures due to the presence of V, which is the slowest diffusing species in this alloy.

Fig. 2(b) displays the microhardness evolution during isochronal aging treatments. Before the main peak at 325 °C alloy Q1 exhibits peaks at 250 and 350 °C, in agreement with those found for the conductivity in Fig. 2(a), thereby confirming the distinct precipitation of Er and Sc, respectively. Alloy Q2 displays a single, wider peak that commences at 300 °C, indicating that the V addition decreases the precipitation kinetics of Er and Sc, as is also visible in Fig. 2(a). Both alloys reach maximum microhardness value at 425 °C, with the peak microhardness of alloy Q2 being 30 MPa greater than alloy Q1 i.e. 565 vs. 535 MPa. However, after the next aging treatment at 450 °C, the microhardness of Q1 decreases precipitously. In comparison, alloy Q2 largely retains its peak microhardness beyond 425 °C till 475 °C, which corresponds to an improvement of more than one 25 °C isothermal step. This retention of high microhardness beyond peak microhardness temperature confirms slower precipitation, coarsening, and dissolution kinetics caused by V.

3.3. Isothermal aging treatments

Fig. 3(a) and (b) display the evolution of electrical conductivity and microhardness for alloys Q1 and Q2 upon isothermal aging at 400 °C. As observed in Fig. 3(a), for both alloys, the conductivity
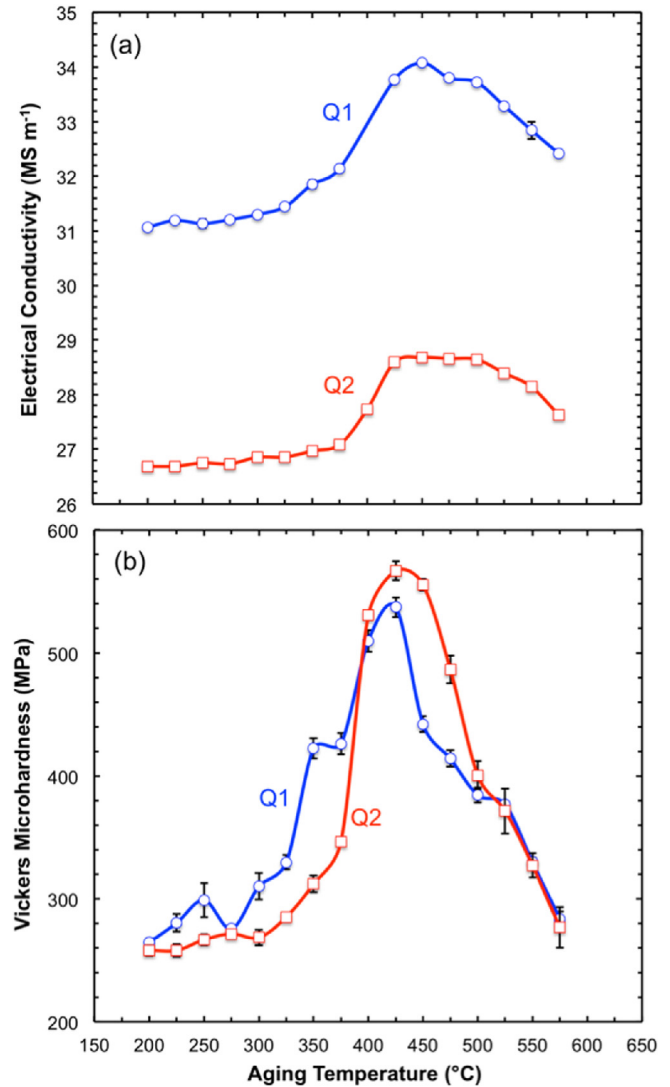
Fig. 2. Plots showing (a) electrical conductivity and (b) Vickers microhardness evolution in alloys Q1 and Q2 during isochronal aging. Samples were held for 3 h at each aging step. Some error bars are not visible since the range is smaller than the marker size.

increases steadily from 1 h through the longest aging time of 264 h, indicating continuous precipitation. A decrease in the slope of the conductivity was observed between 16 and 24 h, marking the onset of coarsening. The same 4–5 MS m^{-1} difference between alloys Q1 and Q2 is observed for isochronal aging treatments (Fig. 2(a)). Fig. 3(b) demonstrates that both alloys have a peak in microhardness after 24 h of aging, with alloy Q1 having a microhardness value 40 MPa greater than alloy Q2 (500 vs. 460 MPa). Alloy Q2 retains, however, its peak microhardness through the longest aging time tested, 264 h, whereas the microhardness of alloy Q1 decreases sharply after 24 h, achieving a value close to the homogenized state after 264 h. This again demonstrates the coarsening resistance of the V-containing alloy.

Fig. 4(a) and (b) display the evolution of conductivity and microhardness for alloys Q1 and Q2 at the higher aging temperature, 425 °C. The conductivity of both alloys evolve in nearly the same manner as observed at 400 °C, except for a shift by a factor of ~2 along the logarithmic time axis. In terms of microhardness, alloy Q2 displays a similar behavior to the trend observed during the

treatment at 400 °C, achieving the same peak microhardness of 450 MPa after 48 h. The first peak observed at 8 h is potentially due to experimental error or sample-to-sample variation, so greater time resolution sampling is required between 5 and 15 h to confirm its presence. By contrast, alloy Q1 fails to achieve the same values of microhardness that it reached at 400 °C. This is probably due to the smaller precipitate number densities obtained at this higher temperature. Alloy Q1 does not, however, exhibit the strong loss of microhardness displayed at 400 °C after 72 h. This may be attributed to faster diffusion of Zr at 425 °C towards the precipitates, hence, increasing their Zr/Sc ratio and improving their coarsening resistance at this temperature. The dendritic structure of these alloys causes local variations in composition, which explains the relatively large distribution in hardness results indicated by the sizeable error bars.

3.4. Double aging treatments

The double-aging treatments were performed to achieve optimal microhardness, as was previously obtained with Al-Er-Sc-Zr alloys [7]. The first stage of the double-aging treatments was performed either at 300 or 350 °C for 16 h, to achieve a high number density of precipitates containing mainly the faster diffusing elements Er and Sc. This first-stage treatment was then followed by a secondary aging step at 400, 425, or 450 °C for times up to 200 h, to achieve subsequent precipitation of the slower diffusing elements Zr and V. The results for alloys Q1 and Q2 are plotted in Fig. 5(a)–(c), respectively, for these three temperatures. Fig. 5(a) displays the microhardness evolution for a secondary aging temperature of 400 °C, where the four curves correspond to alloys Q1 and Q2 subjected to a primary aging treatment at either 300 or 350 °C. All four alloys achieved a peak microhardness after ~12−24 h, which is almost constant within experimental error up to ~100 h aging and at longer aging times, through 200 h, it displays a slight decrease. Alloy Q2 aged initially at 350 °C/16 h performed better than the other cases, achieving a peak microhardness value of 580 MPa and maintaining a value of 540 MPa after 200 h at 400 °C. As observed in Fig. 5(b) and (c), increasing the secondary aging temperature to 425 or 450 °C reduces, for both alloys, the maximum peak microhardness values and the plateaus' duration, but the highest peak microhardness is again associated with alloy
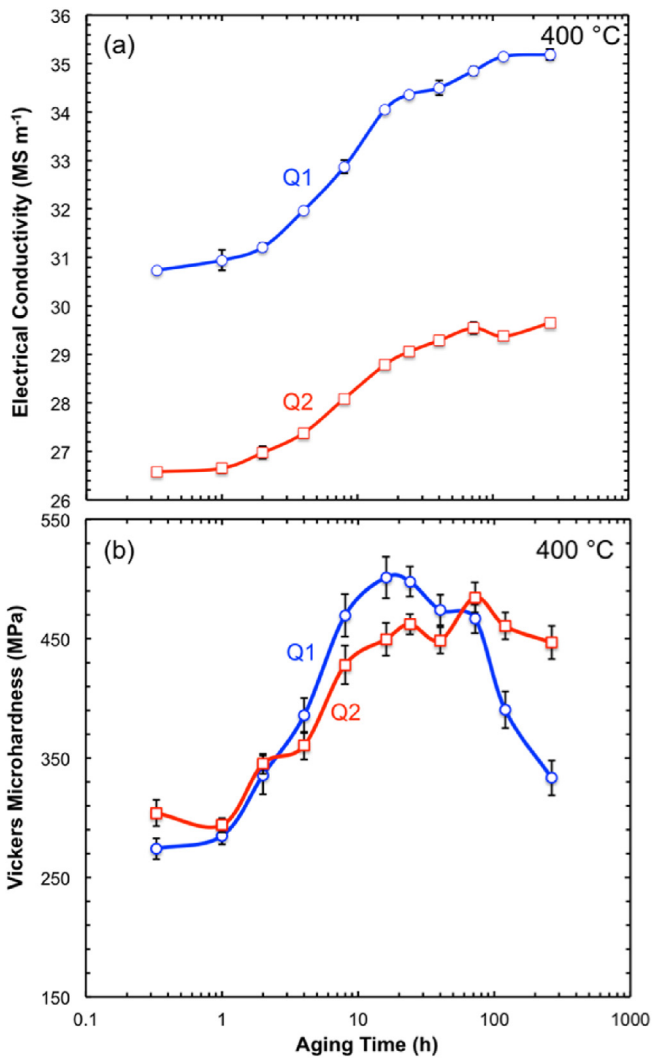
Fig. 3. Plots showing (a) electrical conductivity and (b) Vickers microhardness evolution in alloys Q1 and Q2 during isothermal aging treatments at 400 °C. Some error bars are not visible since the range is smaller than the marker size.
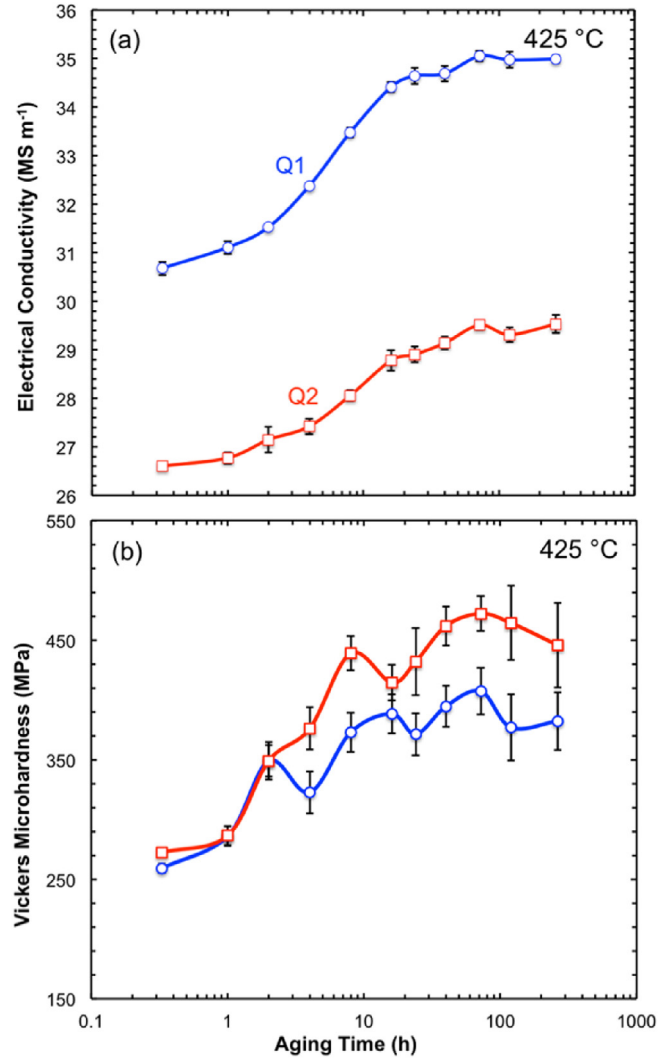
Fig. 4. Plots showing (a) electrical conductivity and (b) Vickers microhardness evolution in alloys Q1 and Q2 during isothermal aging treatments at 425 °C. Some error bars are not visible since the range is smaller than the marker size.

Q2 initially aged at 350°C/16 h and subsequently subjected to a secondary aging treatment at 400 °C for 12 h (a similar micro-hardness value was achieved after 24 h within the error limits). Hence, this aging treatment is selected as the peak aging treatment in the following sections.

3.5. Precipitate nanostructure

Homogenized, peak-aged, and over-aged samples were analyzed using TEM to identify the precipitates' nanostructure and morphology. Dark-field and bright-field TEM images of the homogenized (640 °C/4 h) alloy Q1 presented in Fig. 6(a) and (b) indicate precipitates (marked in red circles) with a mean radius of ~34 ± 9 nm distributed throughout the matrix. Fig. 6(c) displays a bright-field TEM image of the homogenized alloy Q2 (640 °C/4 h), which also shows precipitates distributed in the Al matrix; they were, however, much smaller in comparison to precipitates in the alloy Q1, with a mean radius of ~8 ± 4 nm. The Al-matrix also contains multiple dislocation tangles interacting with these precipitates. It is concluded that the homogenization treatment was not completely effective in eliminating the primary precipitates formed during solidification, due to slow diffusivity of Zr and/or V. The variations in precipitate sizes between these two homogenized alloys might be due to the presence of V in Q2 or due to the compositional variations in samples analyzed, resulting from the segregation of Zr and V (both peritectic elements in Al) into the dendritic cores during solidification.

Fig. 6(d) and (e) display bright-field TEM micrographs of the peak-aged (350 °C/16 h plus 400 °C/12 h) alloys Q1 and Q2, respectively, after homogenization. Both alloys exhibit two distinct sizes of precipitates distributed throughout the Al-matrix. The smaller precipitates (mean radius < 3 nm) are labeled Type 1 and the larger precipitates are labeled Type 2, hereafter. Type 1 precipitates have a mean radius of ~1.4 ± 0.4 nm for alloy Q1 and ~1.8 ± 0.4 nm for alloy Q2, measured in various TEM micrographs at higher magnifications (not shown here). Type 2 precipitates have a mean radius of ~5 ± 1.5 nm for the alloy Q1 and ~28 ± 5 nm for the alloy Q2. Type 2 precipitates in the alloy Q2 are significantly larger than the ones in the alloy Q1, while maintaining a similar mean radius for Type 1 precipitates. Alloy Q1 is expected to show higher solubility for Zr at the homogenization temperature (since V is expected to decrease the solubility of Zr in alloy Q2), so upon quenching and aging, the supersaturation of Zr in the Al matrix is higher in alloy Q2, leading to a higher thermodynamic driving force for precipitation during aging, which results in a higher number density, thus smaller precipitate size. However, the observation of larger Type 2 precipitates in alloy Q2 is not consistent with this hypothesis, which may be due to the compositional variation from the solute segregation on solidification, as mentioned above. Also due to slower transformation kinetics in the V-containing alloy, 4 h at 640 °C was insufficient to dissolve the primary precipitates during homogenization. Additionally, Type 1 precipitates in the alloy Q2 serve as the main dislocation pinning points. Finally, both peak-aged alloys have a much higher number density (number per unit area) of precipitates than in their homogenized states. However, once again, sample-to-sample compositional variations stemming from the dendritic microstructure might be affecting the precipitate evolution in either of these alloys.

Fig. 6(f) and (g) display bright-field TEM micrographs of the over-aged (350 °C/16 h plus 450 °C/24 h) alloys Q1 and Q2, respectively, after homogenization. For both alloys, no clear size distinction is observed for the precipitates in their peak-aged conditions. Both alloys display similar precipitate radii with a mean radius of ~3.7 ± 1.7 nm for the alloy Q1 and a mean radius of ~3.6 nm ± 1.7 for the alloy Q2. The alloy Q2 exhibits a larger
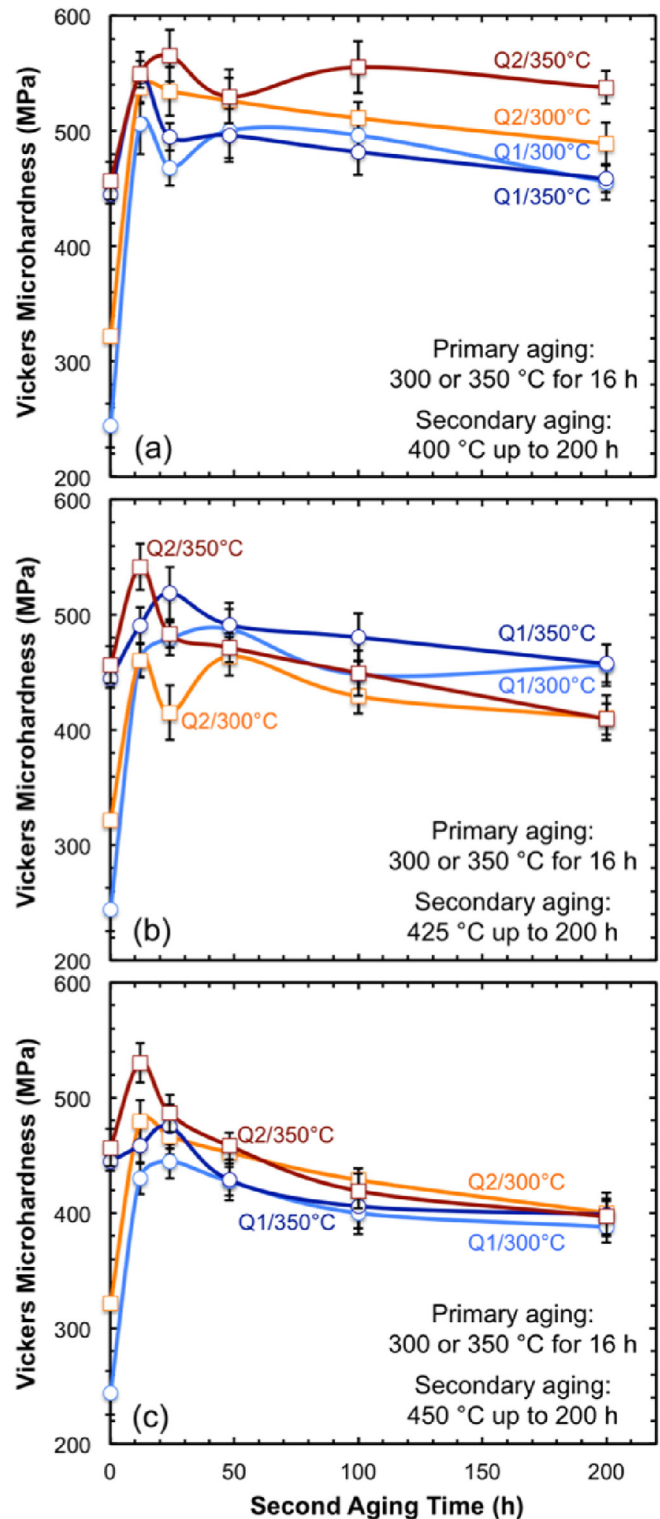

Fig. 5. Vickers microhardness evolution of alloys Q1 and Q2 during double aging treatments, which were performed at a primary aging temperature of 300 or 350 °C for 16 h and a secondary aging temperature of (a) 400, (b) 425, and (c) 450 °C for times up to 200 h.

precipitate number density (number per area) compared to the alloy Q1. This observation confirms that at an aging temperature of 450 °C, V is more effective in preventing dissolution of precipitates than in the absence of V.
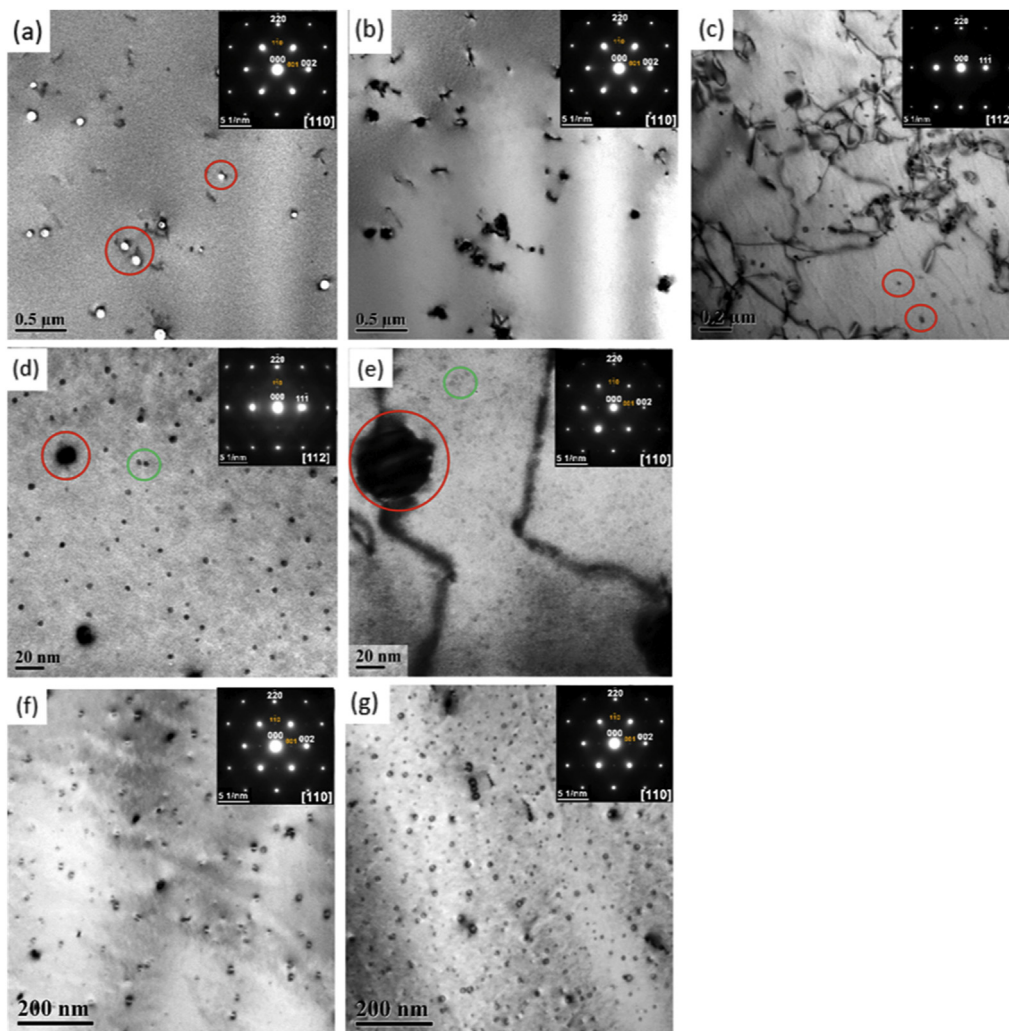
Fig. 6. (a) Dark-field TEM micrograph of alloy Q1 in homogenized condition and corresponding SAED pattern clearly showing the presence of $L1_2$ precipitates (circled in red), (b) corresponding bright-field TEM micrograph of alloy Q1 in homogenized condition with similar SAED pattern, (c) bright-field TEM micrograph of alloy Q2 homogenized condition with multiple dislocation tangles with precipitates (circled in red) in the matrix however $L1_2$ precipitates are not observed in SAED pattern. Bright-field TEM micrographs of (d) alloy Q1 in peak-aged condition; (e) alloy Q2 peak-aged condition, showing two distinct sizes of precipitates (circled in red and green) in both alloys, (f) alloy Q1 in over-aged condition, and (g) alloy Q2 in over-aged condition. Insets show the corresponding selected area diffraction patterns with $L1_2$ precipitates. (For interpretation of the references to colour in this figure legend, the reader is referred to the web version of this article.)

Selected-area electron diffraction (SAED) patterns of alloys Q1 and Q2 for all the above aging treatments are displayed as insets in Fig. 6(a) through 6(g). In all cases, except for the homogenized alloy Q2 (Fig. 6(c)), the $L1_2$-ordered phase is observed, which is distinguishable by the minor diffraction spots (labeled in orange) in between the main FCC diffraction spots. These minor diffraction spots originate from the coherent precipitates in the Al-matrix. The homogenized alloy Q2 (Fig. 6(c)) had no order diffraction spots from the $L1_2$ structure due to the lack of precipitates present in the matrix. The alloys Q1 and Q2 in the peak-aged condition, Fig. 6(d) and (e), contained both Type 1 and Type 2 precipitates with $L1_2$-ordered structure.

To analyze the nano-precipitates and determine the effect of V on their nanostructures, APT experiments were performed on peak- and over-aged samples from alloy Q2. Fig. 7 shows the distribution of all alloying elements in the three-dimensional (3D) reconstruction of the nanotip in the peak-aged condition. The 3D reconstruction displays precipitates with a ~1.3 nm mean radius, enriched in Er, Sc, and Zr, while V is present in the precipitates and

the Al-matrix. To better visualize the partitioning behavior of all alloying elements, a proximity histogram [22,23] was generated based on 62 full and 59 partial precipitates and is displayed in Fig. 8. The core-shell precipitate structure expected for this alloy is apparent in the reconstructed image of a larger full precipitate and the proximity histogram displays higher Zr concentrations in the shell, and higher Er and Sc concentration closer to, and at, the core. The V concentration in the Al-matrix is ~0.10 at.% and reaches a peak value of ~0.30 at.% at the precipitate Zr-rich outer shell, dropping to 0 at.% within 0.5 nm into the precipitate. A similar enrichment of V at the $Al_3(Sc,V)$ precipitate/matrix interface was observed in an arc-melted Al-Sc-V alloy isochronally aged to 400 °C [24]. This is consistent with the fact that V promotes the formation of $L1_2$-ordered $Al_3(Zr,V)$ precipitates [17]. The observed V interfacial enrichment may explain the slower coarsening kinetics of the alloy Q2 because V is a slower diffuser than all the other elements present in the precipitates. It is also known that Al_3V has a lower lattice parameter than Al [18], unlike Al_3Zr, Al_3Sc, and Al_3Er. Thus, small additions of V in the $Al_3(Er,Sc,Zr)$ precipitates will reduce lattice
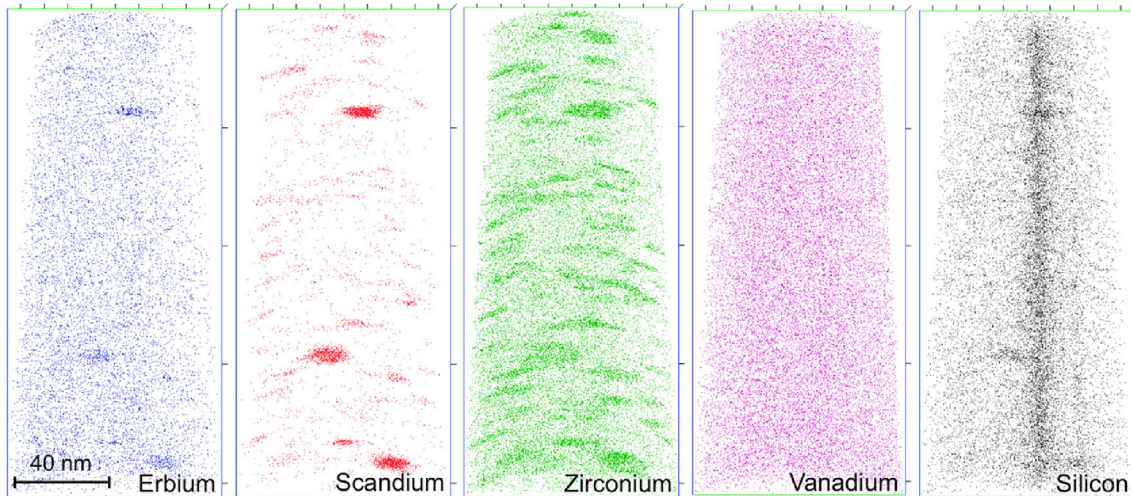
Fig. 7. Atom-probe tomographic elemental distributions for alloy Q2 in the peak-aged condition (350 °C/16 h + 400 °C/12 h).

mismatch with the Al-matrix which may impact both coarsening and creep resistance in the alloy.

Fig. 9 shows the distribution of alloying elements in over-aged alloy Q2, which clearly shows the formation of a core-shell precipitate where an Er- and Sc-rich core is surrounded with a Zr-rich shell. This can be observed in the proxigrams given in Fig. 10, generated based on 3 full and 8 partial precipitates, which also show that Si partitions to the precipitates. The precipitates have a mean radius of 6 nm with an average volume fraction of 0.6% (Table 3). No V segregation at the precipitate/matrix interface is

visible, unlike what is observed in the peak-aged alloy (Fig. 8). However, compositional analysis (summarized in Table 2) shows that this tip is strongly depleted in V (0.02 at.% compared to 0.08 at.% in the bulk alloy), probably because of elemental segregation during dendritic solidification, which is not erased for the slow diffusing elements (i.e., Zr and V) during homogenization. This low V concentration is likely below the solubility limit, and thus V did not precipitate from the solid solution.

Another dataset obtained from a second tip from the same over-aged alloy Q2 illustrates the above hypothesis. Fig. 11 shows
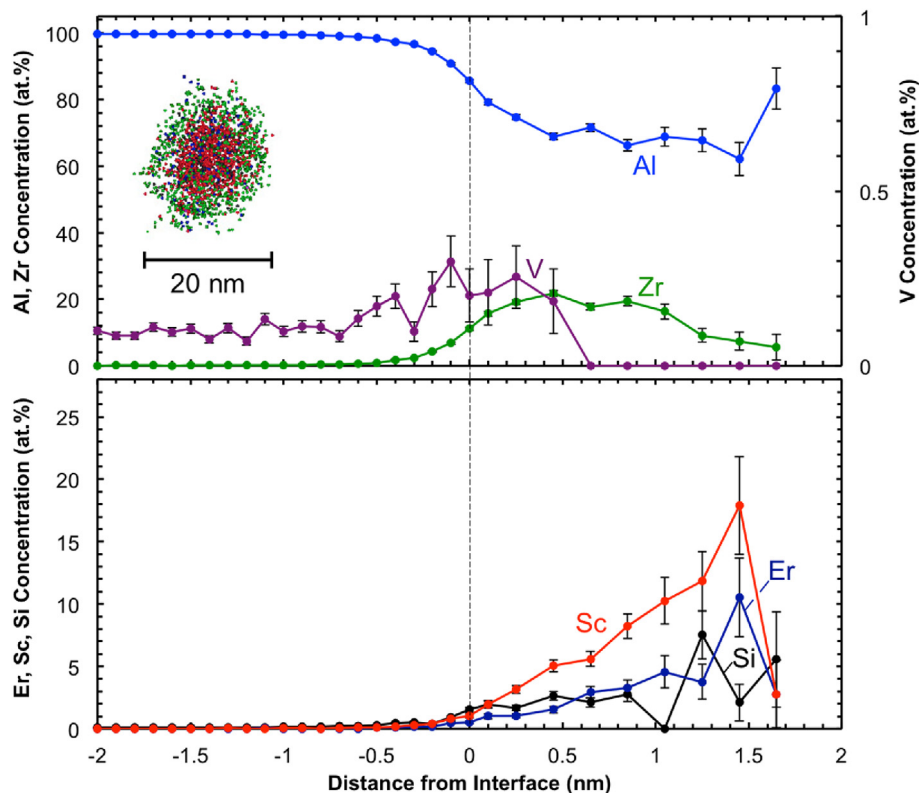

Fig. 8. Proximity histogram of the precipitates in alloy Q2 in the peak-aged condition (350 °C/16 h + 400 °C/12 h). A tomographic image of a larger full precipitate is given as an inset.
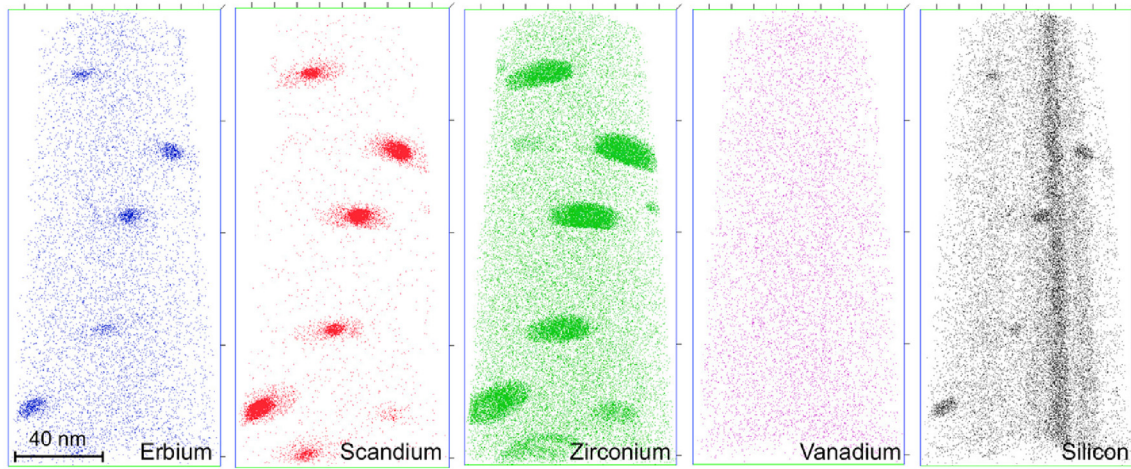
Fig. 9. Atom-probe tomographic elemental distributions for alloy Q2 in the over-aged condition (350 °C/16 h + 450 °C/24 h). This tip was low in V and high in Er.

the elemental distribution sampled from the same specimen as Figs. 9 and 10 (first tip). This second tip reveals precipitates without a core-shell structure, very likely due to the limited amount of Er in the volume (one tenth of the verified composition and one twentieth of the first tip). Instead, co-precipitation of Sc and Zr is observed with a mean precipitate radius of 3 nm (Table 3). This tip has a V concentration of 0.16 at.% (twice as much compared to verified bulk composition) along with 0.2 at.% of Zr (almost three times as much compared to verified bulk composition). These higher Zr and V concentrations are consistent with the segregation due to peritectic solidification. As

shown in Table 2, V is now present in both matrix and precipitate at roughly the same concentration. However, in the precipitates, all the V is near the matrix/precipitate interface (as observed in the peak-aged Q2 specimen, Fig. 8), and the V concentration locally increases to ~0.4 at.%, as shown in the proxigram given in Fig. 12, which was generated based on 3 full and 5 partial precipitates.

3.6. High temperature creep behavior

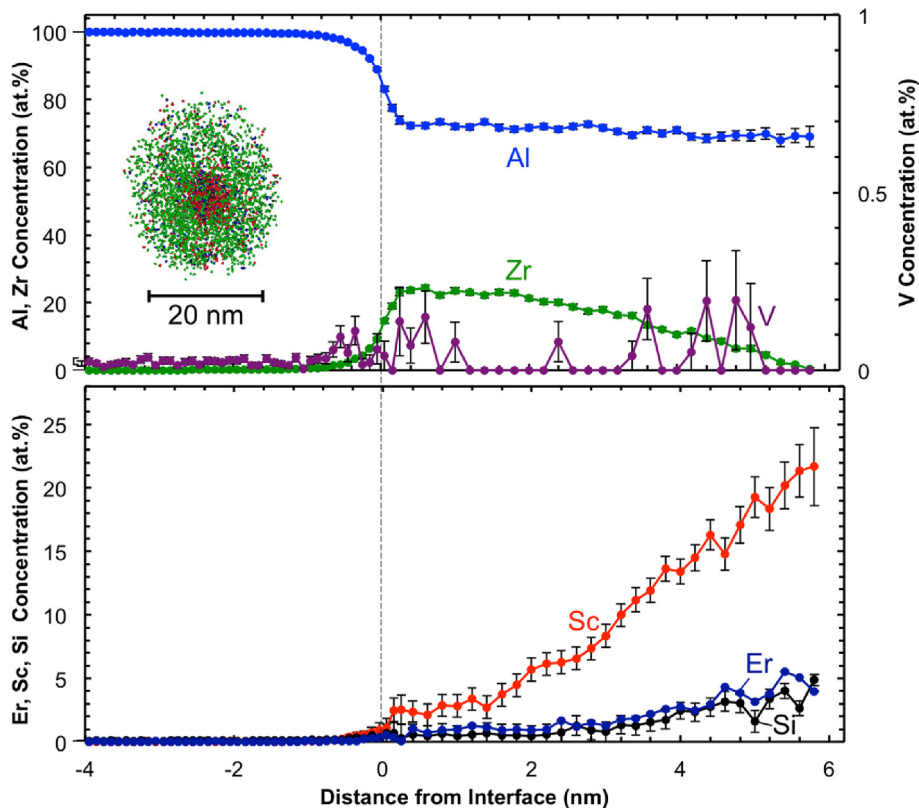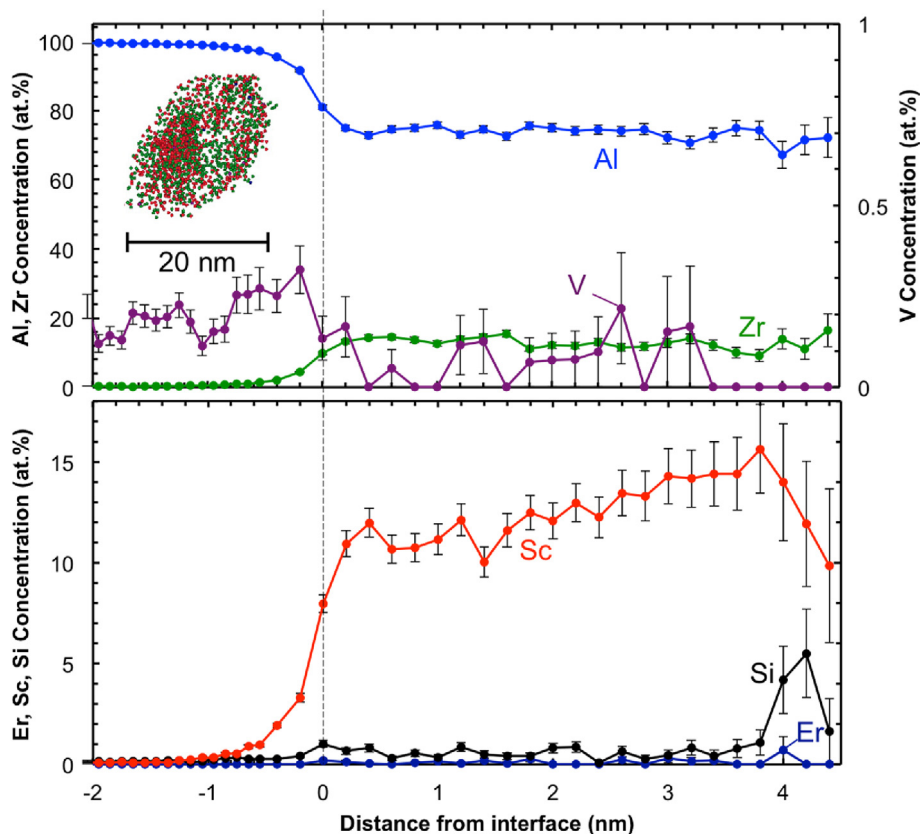Fig. 13 shows the creep behavior at 400 °C for the alloys Q1 and

Fig. 10. Proximity histogram of the precipitates in alloy Q2 in the over-aged condition (350 °C/16 h + 450 °C/24 h). A tomographic image of a larger full precipitate is given as an inset. This tip was low in V and high in Er.

Table 3
Summary of mean radius, number density, and volume fraction data obtained via APT for peak- and over-aged alloy Q2 tips.

	Peak aged	Over aged DS#1	Over aged DS#2
Mean radius	1.34 ± 0.64 nm	6.06 ± 0.66 nm	2.86 ± 1.40 nm
Number density	$9.64 \times 10^{22} \pm 9.8 \times 10^{21}$ m^{-3}	$6.85 \times 10^{21} \pm 2.6 \times 10^{21}$ m^{-3}	$1.44 \times 10^{22} \pm 6.2 \times 10^{21}$ m^{-3}
Volume fraction	0.2713 ± 0.028%	0.5934 ± 0.224%	0.3704 ± 0.158%
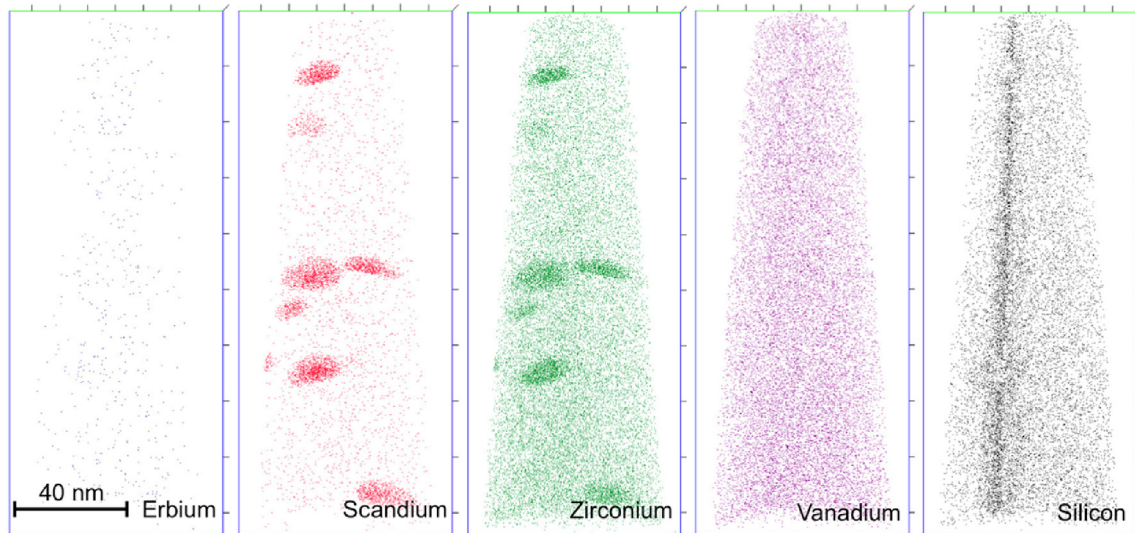
Fig. 11. Atom-probe tomographic elemental distributions for alloy Q2 in the over-aged condition (350 °C/16 h + 450 °C/24 h). This tip was low in Er and high in Zr and V.

Q2 for two different aging conditions: (i) peak aging condition at 350 °C/16 h plus 400 °C/12 h; and (ii) over aging condition at 350 °C/16 h plus 450 °C/24 h. The results suggest that V neither improves nor worsens the creep properties of this alloy at this temperature, as evidenced by a threshold stress of 7.5−8 MPa for all samples. Both under peak and over aging conditions, two alloys exhibit similar resistance to dislocation creep at 400 °C. As previously noted, V is expected to reduce the lattice parameter mismatch between matrix and the precipitates, which could have resulted in poorer creep resistance. When compared to another Al-Er-Sc-Zr-Si alloy [9] both alloys Q1 and Q2 have a slightly lower creep resistance, however, the reference alloy has twice as much Er and 2.5 times more Sc, which more than doubles its price (dictated by Sc) with only a modest gain in creep resistance.

4. Summary and conclusions

The effects of vanadium on the microstructural evolution and high-temperature mechanical behavior of an Al−0.005Er−0.02Sc−0.07Zr−0.06Si at.%. alloy are investigated. The following conclusions are reached based on the experimental results:

1. As-cast alloys have a relatively coarse grain structure, which is desirable for optimal creep resistance. Primary Al_3Zr precipitates are observed at the grain boundaries after homogenization at 640 °C for 4 h.
2. Isochronal aging treatments reveal that the V-containing alloy Q2 has slower precipitation and coarsening kinetics when compared to the V-free alloy Q1 as demonstrated by microhardness and electrical conductivity measurements. However, the alloy Q2 still achieves a higher peak microhardness value.

3. Isothermal aging treatments are performed at 400 and 425 °C for durations up to 264 h. The results demonstrate, once again, slower precipitation and coarsening kinetics for the V-containing alloy at both temperatures. Even though the V-free alloy Q1 reaches a higher peak microhardness at 400 °C, the microhardness decreases sharply after 24 h at this temperature, while the V-containing alloy Q2's microhardness remains relatively constant up to 264 h.
4. Double-aging studies are performed at a primary aging temperature of 300 or 350 °C for 16 h and a secondary aging-temperature of 400, 425, or 450 °C for durations up to 200 h. The V-containing alloy Q2 demonstrates a higher microhardness, which remains relatively stable as a function of aging duration for each secondary aging-temperature. The peak aging condition obtained based on these studies is 350 °C/16 h plus 400 °C/12 h double aging treatment.
5. TEM analyses reveal that the peak-aged alloy Q2 has a mixture of smaller (1.8 nm mean radius) and larger (28 nm mean radius) precipitates. The smaller precipitates were analyzed using atom-probe tomography and proximity histograms (proxigrams) demonstrate that V is mainly situated at the matrix/precipitate interface, most likely forming a precipitate shell, $Al_3(Zr,V)$. The presence of V in the shell, around the core, along with low diffusivity of V reduces the lattice parameter misfit between the matrix and the precipitate, increasing the coarsening resistance as demonstrated by the microhardness measurements.
6. A reduced lattice parameter misfit could have also reduced the creep resistance. However, compressive creep experiments conducted at 400 °C showed no significant difference between V-free alloy Q1 and V-containing alloy Q2 in terms of creep resistance, in either peak-aged or over-aged conditions.

Fig. 12. Proximity histogram of the precipitates in alloy Q2 in the over-aged condition (350 °C/16 h + 450 °C/24 h). A tomographic image of a larger full precipitate is given as an inset. This tip was low in Er and high in Zr and V.
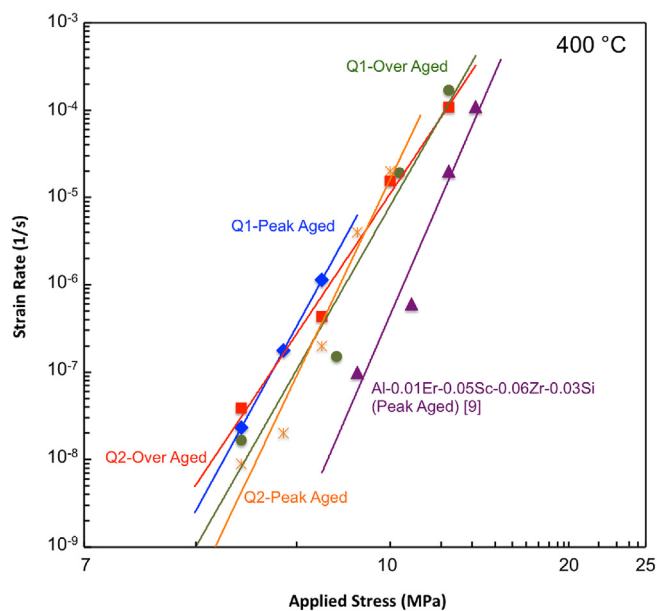
Fig. 13. Creep properties of alloys Q1 and Q2 under compressive stresses at 400 °C for peak-aged (350 °C/16 h + 400 °C/12 h) or over-aged (350 °C/16 h + 450 °C/24 h) conditions. Creep data of a similar alloy (Al-0.01Er-0.05Sc-0.06Zr-0.03Si) are also plotted for comparison purposes [9].

Overall, the Al-Er-Sc-Zr-V-Si alloy investigated in this study exhibits improved coarsening resistance at elevated temperatures with no apparent reduction in the creep resistance at 400 °C.

References

[1] J. Royset, N. Ryum, Scandium in aluminium alloys, Int. Mater. Rev. 50 (2005) 19–44.

[2] K.E. Knipling, D.C. Dunand, D.N. Seidman, Criteria for developing castable, creep-resistant aluminum-based alloys - a review, Z. Fur Met. 97 (2006) 246–265.

[3] R.A. Karnesky, M.E. van Dalen, D.C. Dunand, D.N. Seidman, Effects of substituting rare-earth elements for scandium in a precipitation-strengthened Al-0.08 at.% Sc alloy, Scr. Mater. 55 (2006) 437–440.

[4] K.E. Knipling, R.A. Karnesky, C.P. Lee, D.C. Dunand, D.N. Seidman, Precipitation evolution in Al-0.1Sc, Al-0.1Zr and Al-0.1Sc-0.1Zr (at.%) alloys during isochronal aging, Acta Mater. 58 (2010) 5184–5195.

[5] O. Beeri, D.C. Dunand, D.N. Seidman, Roles of impurities on precipitation kinetics of dilute Al-Sc alloys, Mater. Sci. Eng. A Struct. Mater. Prop. Microstruct. Process. 527 (2010) 3501–3509.

[6] K.E. Knipling, D.N. Seidman, D.C. Dunand, Ambient- and high-temperature mechanical properties of isochronally aged Al-0.06Sc, Al-0.06Zr and Al-0.06Sc-0.06Zr (at.%) alloys, Acta Mater. 59 (2011) 943–954.

[7] C. Booth-Morrison, D.C. Dunand, D.N. Seidman, Coarsening resistance at 400 degrees C of precipitation-strengthened Al-Zr-Sc-Er alloys, Acta Mater. 59 (2011) 7029–7042.

[8] C. Booth-Morrison, Z. Mao, M. Diaz, D.C. Dunand, C. Wolverton, D.N. Seidman, Role of silicon in accelerating the nucleation of $Al_3(Sc,Zr)$ precipitates in dilute Al-Sc-Zr alloys, Acta Mater. 60 (2012) 4740–4752.

[9] C. Booth-Morrison, D.N. Seidman, D.C. Dunand, Effect of er additions on ambient and high-temperature strength of precipitation-strengthened Al-Zr-Sc-Si alloys, Acta Mater. 60 (2012) 3643–3654.

[10] N.Q. Vo, D.C. Dunand, D.N. Seidman, Improving aging and creep resistance in a dilute Al-Sc alloy by microalloying with Si, Zr and Er, Acta Mater. 63 (2014) 73–85.

[11] R.A. Karnesky, D.C. Dunand, D.N. Seidman, Evolution of nanoscale precipitates in Al microalloyed with Sc and Er, Acta Mater. 57 (2009) 4022–4031.

[12] M.E. van Dalen, R.A. Karnesky, J.R. Cabotaje, D.C. Dunand, D.N. Seidman, Erbium and ytterbium solubilities and diffusivities in aluminum as determined by nanoscale characterization of precipitates, Acta Mater. 57 (2009) 4081–4089.

[13] Y. Harada, D.C. Dunand, Microstructure of Al_3Sc with ternary rare-earth additions, Intermetallics 17 (2009) 17–24.

[14] M.E. Krug, A. Werber, D.C. Dunand, D.N. Seidman, Core-shell nanoscale precipitates in Al-0.06 at.% Sc microalloyed with Tb, Ho, Tm or Lu, Acta Mater. 58 (2010) 134–145.

[15] S. Chen, C. Li, G. Lian, C. Guo, Z. Du, Effect of elastic strain energy on the core-shell structures of the precipitates in Al-Sc-Er alloys, J. Rare Earths 30 (2012) 1276–1280.

[16] Y. Harada, D.C. Dunand, Microstructure of Al(3)Sc with ternary transition-metal additions, Mater. Sci. Eng. A Struct. Mater. Prop. Microstruct. Process. 329 (2002) 686–695.

[17] Y.C. Chen, M.E. Fine, J.R. Weertman, R.E. Lewis, Coarsening behavior of $L1_2$ structured $Al_3(Zr_x,V_{1-x})$ precipitates in rapidly solidified Al-Zr-V alloy, Scr. Metall. 21 (1987) 1003–1008.

[18] M.S. Zedalis, M.E. Fine, Precipitation and ostwald ripening in dilute Al base-Zr-V alloys, Metall. Trans. A Phys. Metall. Mater. Sci. 17 (1986) 2187–2198.

[19] D.N. Seidman, Three-dimensional atom-probe tomography: advances and applications, Annu. Rev. Mater. Res. 37 (2007) 127–158.

[20] D.N. Seidman, K. Stiller, An atom-probe tomography primer, MRS Bull. 34 (2009) 717–724.

[21] S. Park, N.Q. Vo, D.N. Seidman, D.C. Dunand, Unpublished Work, Northwestern University, 2014.

[22] O.C. Hellman, J.A. Vandenbroucke, J. Rusing, D. Isheim, D.N. Seidman, Analysis of three-dimensional atom-probe data by the proximity histogram, Microsc. Microanal. 6 (2000) 437–444.

[23] J. Rusing, J.T. Sebastian, O.C. Hellman, D.N. Seidman, Three-dimensional investigation of ceramic/metal heterophase interfaces by atom-probe microscopy, Microsc. Microanal. 6 (2000) 445–451.

[24] K.E. Knipling, The effect of group 5 (V, Nb, Ta) additions on precipitation in Al-Sc alloys, Microsc. Microanal. 22 (2016) 688–689.